Structure and mechanism of IFN-γ antagonism by an orthopoxvirus IFN-γ-binding protein

Anthony A. Nuara*†, Leigh J. Walter*, Naomi J. Logsdon*, Sung Il Yoon*‡, Brandi C. Jones*, Jill M. Schriewer†, R. Mark Buller†, and Mark R. Walter*‡§

*Center for Biophysical Sciences and Engineering and ‡Department of Microbiology, University of Alabama at Birmingham, Birmingham, AL 35294; and †Department of Molecular Microbiology and Immunology, Saint Louis University Health Sciences Center, St. Louis, MO 63104

Edited by Theodore Jardetzky, Howard Hughes Medical Institute, Northwestern University, Chicago, IL, and accepted by the Editorial Board December 12, 2007 (received for review June 19, 2007)

Ectromelia virus (ECTV) encodes an IFN-γ-binding protein (IFN-γBP^{ECTV}) that disrupts IFN-γ signaling and its ability to induce an antiviral state within cells. IFN-γBP^{ECTV} is an important virulence factor that is highly conserved (>90%) in all orthopoxviruses, including variola virus, the causative agent of smallpox. The 2.2-Å crystal structure of the IFN-γBP^{ECTV}/IFN-γ complex reveals IFN-γBP^{ECTV} consists of an IFN-γR1 ligand-binding domain and a 57-aa helix-turn-helix (HTH) motif that is structurally related to the transcription factor TFIIA. The HTH motif forms a tetramerization domain that results in an IFN-γBP^{ECTV}/IFN-γ complex containing four IFN-γBP^{ECTV} chains and two IFN-γ dimers. The structure, combined with biochemical and cell-based assays, demonstrates that IFN-γBP^{ECTV} tetramers are required for efficient IFN-γ antagonism.

ectromelia virus | immunomodulator | interferon | cytokine | complex

Ectromelia virus (ECTV) is an orthopoxvirus that causes mousepox, which closely resembles the genetic and disease characteristics of the human pathogen variola virus (VARV), the causative agent of smallpox (1). The genomes of all orthopoxviruses, including ECTV and VARV, encode proteins required for viral replication, as well as soluble cytokine- and chemokine-binding proteins, which disrupt the activation and recruitment of immune cells responsible for host antiviral responses (2, 3). The severity of smallpox and mousepox has been attributed to the effectiveness of these immunomodulatory proteins, which in many instances, exhibit significant homology to cellular receptors, suggesting they were captured and adapted to subvert host immune responses during poxvirus evolution.

All orthopoxviruses express IFN-γ-binding proteins (IFN-γBPs) that efficiently block IFN-γ-mediated signaling cascades responsible for activating potent antiviral defense mechanisms. The importance of IFN-γ in viral pathogenesis is demonstrated by studies in C57BL/6 mice, in which depletion of IFN-γ by monoclonal antibody treatment, or disruption of the signaling pathway through genetic means, transforms benign ECTV infection into a lethal one (4, 5). In addition, the ectromelia virus IFN-γBP (IFN-γBP^{ECTV}) has been shown to be a critical virulence factor in BALB/c mice, in which ECTV infections are lethal but infections with an ECTV mutant lacking a functional IFN-γBP^{ECTV} are not (6).

Orthopoxvirus IFN-γBPs are ≈270-aa proteins that share >90% sequence identity with one another and ≈20% sequence identity with the extracellular region of the cellular IFN-γR1 chains, often called the cytokine receptor homology region (CRHR). In contrast to cellular IFN-γR1s, which exhibit species-specific binding to their cognate ligand, IFN-γBPs exhibit relaxed IFN-γ-binding specificity (7, 8) (e.g., IFN-γBP^{ECTV} binds human, murine, rabbit, and bovine IFN-γ). This functional difference may have facilitated opportunistic viral infections in multiple hosts during the evolution of the virus.

In contrast to the CRHR, the C-terminal ≈60 aa of the IFN-γBPs share no identifiable sequence similarity with cellular proteins. Recent studies suggest that the C terminus mediates oligomerization of the IFN-γ-binding domains (9). However, there are conflicting reports about the quaternary structure of the molecules. For example, IFN-γBPs encoded by VACV-WR (Western Reserve) and myxoma virus (M-T7) have been reported to form dimers and trimers, respectively (10, 11). In contrast to these reports, we have demonstrated recently that IFN-γBPs from ECTV and VACV-B8R (Copenhagen strain) adopt larger oligomers in solution, likely tetramers, which are critical for antagonizing IFN-γ activity (9).

To address the basic mechanisms of IFN-γ antagonism by orthopoxvirus IFN-γBPs, we determined the crystal structure of IFN-γBP^{ECTV} bound to human IFN-γ. IFN-γBP^{ECTV} adopted a tetrameric structure that bound two IFN-γ dimers. Biochemical assays confirmed that IFN-γBP^{ECTV} was secreted from infected cells as a tetramer and that this quaternary structure was essential for efficient IFN-γ antagonism. The C terminus of IFN-γBP^{ECTV} was structurally related to the helix-turn-helix (HTH) motif of TFIIA, which functions as a transcription factor oligomerization domain. Furthermore, IFN-γBP^{ECTV} formed extensive interactions with the flexible C terminus of IFN-γ, which provided insights into the relaxed species specificity of the IFN-γBPs.

Results

Architecture of the IFN-γBP^{ECTV} Monomer. The structure of IFN-γBP^{ECTV} was determined at 2.2-Å resolution by using molecular replacement methods and refined to an R_{free} value of 24.5% [supporting information (SI) Table 1]. IFN-γBP^{ECTV} residues 17–210 were structurally similar to the extracellular domain of the human cellular IFN-γR1 chain (Fig. 1). The CRHRs of IFN-γBP^{ECTV} and IFN-γR1 were each composed of two fibronectin type III domains (FBNIII) containing seven conserved β-strands labeled A to G. The rmsd between the N-terminal (D1) and C-terminal (D2) FBNIII domains of IFN-γBP^{ECTV} and IFN-γR1 were 2.0 Å (Cα atoms, 17–100) and 1.9 Å (Cα atoms, 101–214), respectively. The interdomain angles between D1 and D2 domains of IFN-γBP^{ECTV} and IFN-γR1 were both ≈120°.

Amino acid sequences corresponding to the membrane spanning helix and intracellular domain of IFN-γR1 are replaced by a 57-residue peptide in IFN-γBP^{ECTV}. As shown in Fig. 1, the peptide formed an extended linker (residues 211–220), followed

Author contributions: A.A.N., L.J.W., N.J.L., B.C.J., R.M.B., and M.R.W. designed research; A.A.N., L.J.W., N.J.L., S.I.Y., B.C.J., J.M.S., and M.R.W. performed research; A.A.N., L.J.W., S.I.Y., R.M.B., and M.R.W. analyzed data; and R.M.B. and M.R.W. wrote the paper.

The authors declare no conflict of interest.

This article is a PNAS Direct Submission. T.J. is a guest editor invited by the Editorial Board.

Data deposition: The atomic coordinates and structure factors have been deposited in the Protein Data Bank, www.pdb.org (PDB ID codes 3BES and RCSB045439).

§To whom correspondence should be addressed. E-mail: walter@uab.edu.

This article contains supporting information online at www.pnas.org/cgi/content/full/0705753105/DC1.

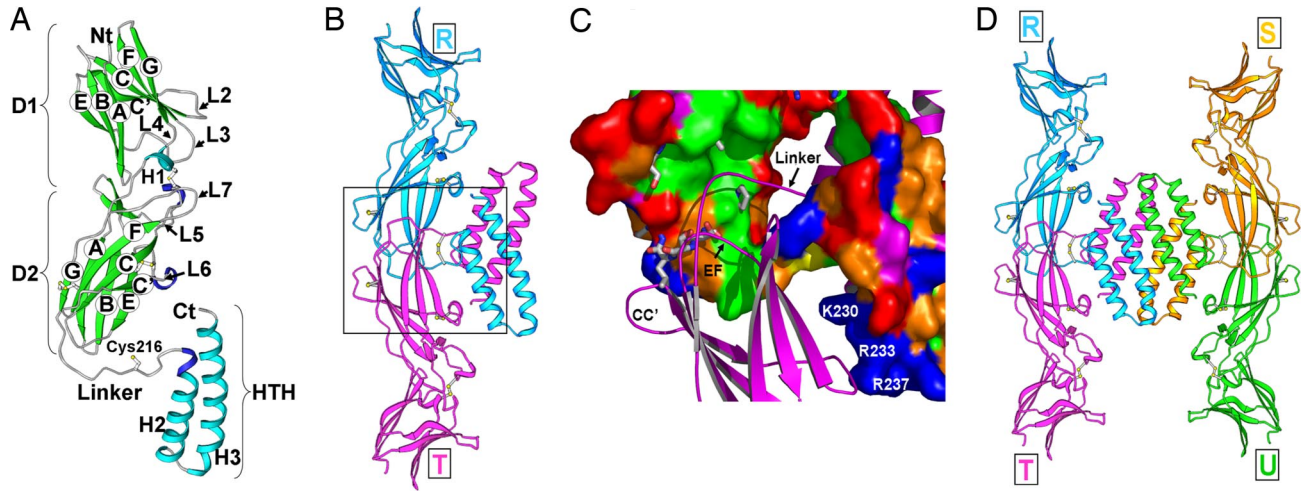

Fig. 1. Structure of IFN-γBP^{ECTV}. (*A*) Ribbon diagram of the IFN-γBP^{ECTV} monomer. (*B*) Ribbon diagram of the IFN-γBP^{ECTV} dimer. Chains R and T are colored cyan and magenta, respectively. (*C*) Close-up of the T/R dimer interface (boxed region in *B*). The molecular surface colored by residue type (D and E, red; K and R, blue; G, magenta; C, yellow; S, T, H, N, and Q, orange; A, P, V, M, L, I, F, and W, green) is shown for chain R. Protruding residues in the EF and CC′ loops of the IFN-γR1 that prevent ''IFN-γBP^{ECTV}-like'' dimerization are shown in stick representation. (*D*) Ribbon diagram of the IFN-γBP^{ECTV} tetramer.

by a HTH motif (Fig. 1*A*). Database searches failed to identify any proteins with amino acid sequence similarity to the HTH motif. However, the IFN-γBP^{ECTV} HTH motif was structurally similar to the HTH motif found in the yeast transcription factor TFIIA (rmsd, ≈1.6 Å; SI Fig. 6), which is critical for the proper assembly of the large and small subunits of the protein (12, 13). Although the individual IFN-γBP^{ECTV} and TFIIA HTH motifs were structurally similar, their quaternary structures were markedly different. The IFN-γBP^{ECTV} HTH formed an eight-helix homotetramer structure (Fig. 1*D*), whereas the TFIIA HTH forms a heterodimer that resembles a four-helix bundle (12, 13).

The IFN-γBP^{ECTV} R/T Dimer. The IFN-γBP^{ECTV} monomer formed an elongated intertwined dimer through extensive interactions between two-fold-related D2, linker, and HTH domains (Fig. 1*B*). The two chains of the dimer were linked by an interchain disulfide bond between two-fold-related Cys-216 residues located in the linker region. A total of 2,317 Å^2 of surface area was buried by each IFN-γBP^{ECTV} monomer upon dimer formation. In the dimer, salt bridge interactions occurred between aspartic acid residues (Asp-165 and Asp-167) located in the D2 domains and Lys-230 and Arg-237 contributed from helix H2 in the two-fold-related HTH motif (Fig. 1*C*). Interestingly, the negatively charged dimer assembly region on the IFN-γBP^{ECTV} D2 domain corresponded to the putative binding site for the positively charged IFN-γ C-terminal tail in IFN-γR1 (14). The highly integrated dimer structure showed that the HTH domains do not simply tether the IFN-γ-binding CRHRs like beads on a string. Rather, the extensive dimer interface locked the two-fold-related IFN-γBP^{ECTV} monomers into an extended rod-like structure.

A comparison of IFN-γBP^{ECTV} and IFN-γR1 revealed that IFN-γBP^{ECTV} dimerization was promoted by sequence and structural differences in the EF and CC′ loops of the D2 domains (Fig. 1*C*). The conformation of the eight-residue IFN-γR1 EF loop sterically prevented D2–D2 dimer formation. However, this steric impediment to dimer formation was removed in IFN-γBP^{ECTV} by shorting the EF loop to five residues. To further promote dimer formation, the conformation of the D2 CC′ loop in IFN-γBP^{ECTV} exposed a hydrophobic patch on D2, which was covered by the loop in IFN-γR1. Together, these changes promoted IFN-γBP^{ECTV} dimerization and the specific orientation observed for the two-fold-related CRHRs (Chains R/T and S/U, Fig. 1*B*).

The IFN-γBP^{ECTV} R/T-S/U Tetramer. IFN-γBP^{ECTV} dimers assembled into tetramers containing four peptide chains (R, S, T, and U) related by 222-point symmetry (Fig. 1*D*). Tetramer formation occurred exclusively through contacts made between residues 238 and 264 (helix H3) of the HTH motifs (Fig. 2). Contacts within the tetramer domain consisted mostly of Van der Waals interactions contributed by hydrophobic and polar amino acids. Reminiscent of the GCN4 coiled coil (15), only one specific hydrogen bond between Asp-257 and Ser-253 in adjacent H3 helices was found at the center of the tetramer (R/U chains and T/S chains) (Fig. 2*A*). Each HTH motif buried 766 Å^2 of accessible surface area into the tetramer for a total of 3,084 Å^2. The extensive amount of buried surface area suggests that IFN-γBP^{ECTV} exists as a highly stable tetramer in the absence of IFN-γ, which is consistent with previous quaternary structure analysis of IFN-γBP^{ECTV} (9).

Mutagenesis of Residues Involved in IFN-γBP^{ECTV} Tetramerization. Previous mutation of IFN-γBP^{ECTV} H3 residues 258–266 individually to alanine has no effect on IFN-γBP^{ECTV} tetramer formation or IFN-γ neutralization (9). Interestingly, eight of these nine residues buried surface area predominantly into the IFN-γBP^{ECTV} dimer interface and not the tetramer interface (Fig. 2*B*). To specifically analyze the tetramer contacts, five additional IFN-γBP^{ECTV} residues, which form the R/T–S/U tetramer interface (Gln-242, Tyr-246, Phe-250, Ser-253, and Asp-257; see Fig. 2), were individually mutated to alanine.

The IFN-γBP^{ECTV} mutants were expressed in CV-1 cells and tested for their ability to block murine IFN-γ (muIFN-γ)-mediated protection of L929 cell monolayers from vesicular stomatitis virus (VSV) infection (SI Fig. 7). With the exception of the Phe250Ala mutation, all IFN-γBP^{ECTV} alanine mutants blocked muIFN-γ antiviral activity almost as efficiently as WT IFN-γBP^{ECTV}, resulting in a large VSV-induced cytopathic effect. The quaternary structure of each IFN-γBP^{ECTV} mutant was also evaluated by size-exclusion chromatography (SEC) (see SI Fig. 8). IFN-γBP^{ECTV}, as well as Gln242Ala, Tyr246Ala, Ser253Ala, and Ser257Ala mutants exhibited tetrameric elution profiles, whereas IFN-γBP^{ECTV} Phe250Ala eluted from the column as a dimer.

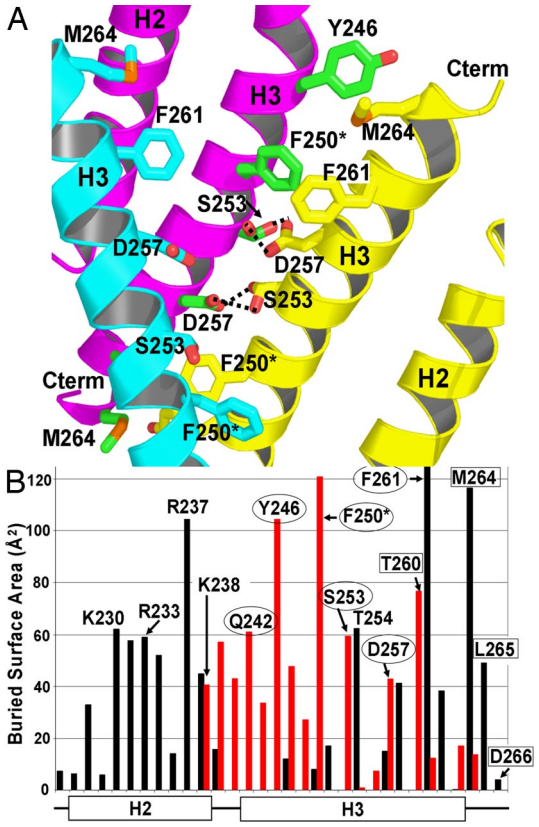

Fig. 2. Structure and function of the HTH tetramer. (*A*) Close-up of R/T HTH dimer (chains R and T) forming one side of the tetramer interaction and HTH chain S colored as described in Fig. 1. (*B*) Surface area buried by each HTH residue in the IFN-γBP^{ECTV} dimer (black bars) and tetramer interfaces (red bars). The single alanine mutants tested in this study are circled. The labels for some of the alanine mutants analyzed in other work [residues 258–266 (9)] are boxed. Of the 14 mutants tested, only the Phe250Ala mutation (marked by an asterisk) significantly disrupts IFN-γ neutralization and IFN-γBP^{ECTV} tetramer formation (see SI Figs. 7 and 8).

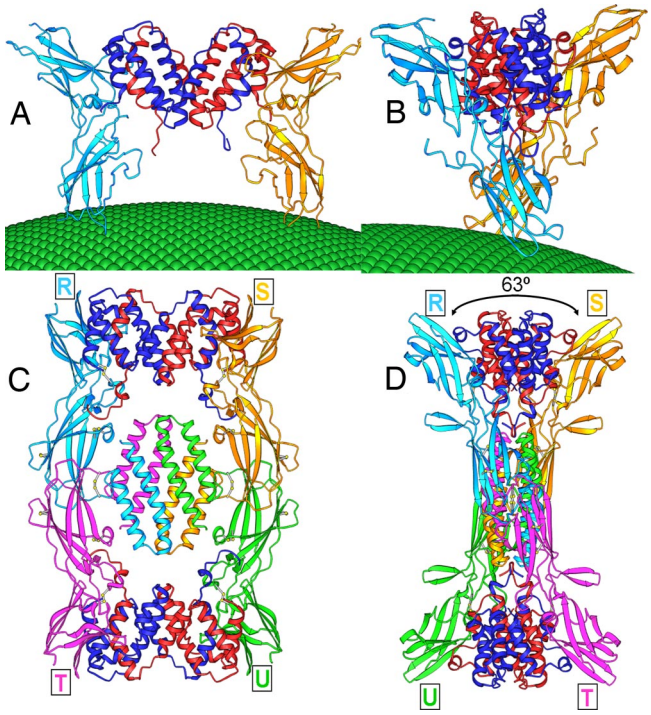

Fig. 3. Comparison of IFN-γ/IFN-γR1 and IFN-γ/ IFN-γBP^{ECTV} complexes. (*A–D*) Orthogonal views of the IFN-γ/IFN-γR1 (*A* and *B*) and IFN-γ/ IFN-γBP^{ECTV} (*C* and *D*) complexes.

The results suggest that IFN-γBP^{ECTV} Phe-250 is critical for IFN-γBP^{ECTV} tetramer formation and IFN-γ antagonism. The importance of Phe-250 is consistent with its location in the HTH motif and the large amount of surface area it buried upon tetramer formation (121 Å^2, e.g., 4 × 121 Å^2 = 484 Å^2 in the tetramer; Fig. 2). To further emphasize the importance of the tetramer contact, versus the more extensive R/T dimer interactions, we reevaluated the functional properties of the IFN-γBP^{ECTV} Phe261Ala mutant (SI Figs. 7 and 8). Phe-261 was chosen because it buried essentially the same amount of surface area as Phe-250 (126 Å^2) but into the R/T and S/U dimer interfaces (Figs. 1*B* and 2). As previously described, the IFN-γBP^{ECTV} Phe261Ala mutation exhibits essentially WT activity and elutes as a tetramer (9).

The IFN-γBP^{ECTV}/IFN-γ Complex. IFN-γBP^{ECTV} R/S and T/U chains (Fig. 1*D*) mimicked the positions of IFN-γR1 in the IFN-γ/IFN-γR1 complex (Fig. 3 *A* and *B*). As a result, each IFN-γBP^{ECTV} tetramer bound two IFN-γ homodimers (Fig. 3 *C* and *D*). The asymmetric unit of the crystals contained one chain of IFN-γ and one chain of IFN-γBP^{ECTV}. Thus, the tetramer complex, comprising four chains of IFN-γ and four chains of IFN-γBP^{ECTV}, was generated by the 222 crystallographic symmetry of the space group. The C-terminal ends of the CRHRs (R/S and T/U chains) were separated by 74 Å compared with ≈84 Å in the IFN-γ/IFN-γR1 complex [PDB ID code 1fg9 (16)]. Viewing the complex from the side (Fig. 3*D*) revealed that the tetramer was not planar. Rather, the R/T and S/U dimers were oriented at an angle of ≈63° with respect to each other, which closely mimicked the orientation of the two-fold-related IFN-γR1 chains in the IFN-γ/IFN-γR1 complex (Fig. 3*B*). The structure revealed IFN-γBP^{ECTV} tetramerization was required to form a bivalent high-affinity IFN-γ-binding site for efficient neutralization of its biological activity.

The IFN-γBP^{ECTV}/IFN-γ-Binding Interface. Interactions between IFN-γBP^{ECTV} and IFN-γ are similar to those previously described in the IFN-γ/IFN-γR1 interface (14, 16, 17). IFN-γBP^{ECTV} residues involved in IFN-γ binding were presented on six different receptor loops (L2 to L7) located at the D1–D2 interface (Fig. 1*A*). IFN-γBP^{ECTV} contacted IFN-γ residues located on helices A, B, and F and the AB loop (Fig. 4). However, in contrast to IFN-γR1, IFN-γBP^{ECTV} formed interactions with the IFN-γ C-terminal tail (residues 128–132; sequence Lys-Arg-Lys-Arg-Ser; Figs. 4 and 5). As a result, interactions between IFN-γBP^{ECTV} and IFN-γ were more extensive than in the IFN-γ/IFN-γR1 complex.

Only 5 of 38 residues used by IFN-γBP^{ECTV} to contact IFN-γ were conserved in IFN-γR1. All five conserved residues (Y47, G48, W52, S76, and W78) were located on the L2 and L3 loops. These residues participated in two conserved hydrogen bonds between L2 residue Tyr-47$^{IFN\text{-}\gamma BP(ECTV)}$ and Glu-112$^{IFN\text{-}\gamma}$ and L3 loop residue Trp-78$^{IFN\text{-}\gamma BP(ECTV)}$ and Gly-18$^{IFN\text{-}\gamma}$ (SI Table 2). One additional interaction between Arg-45$^{IFN\text{-}\gamma BP(ECTV)}$ and Asp-24$^{IFN\text{-}\gamma}$ was similar to the Lys-47$^{IFN\text{-}\gamma R1}$–Asp-24$^{IFN\text{-}\gamma}$ contact in the IFN-γ/IFN-γR1 complex. IFN-γBP^{ECTV} is the only orthopoxvirus IFN-γBP sequenced to date that contains an arginine at position 45, rather than a lysine. Preliminary mutagenesis studies suggest that this amino acid difference is partially responsible for the ability of IFN-γBP^{ECTV}, but not IFN-γBP$^{VACV\text{-}B8R}$, to recognize murine IFN-γ (18).

A total of 33 IFN-γ residues (>3 Å^2) buried 1,448 Å^2 of

BIOCHEMISTRY

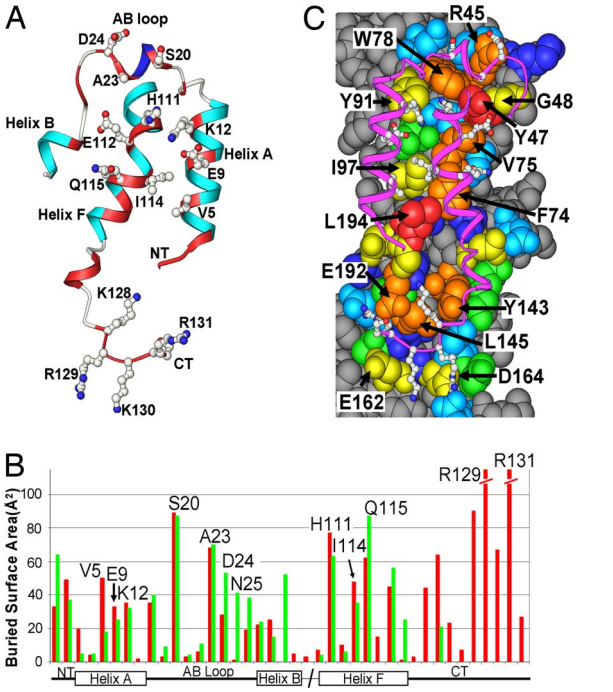

Fig. 4. The IFN-γ/IFN-γBP^{ECTV}-binding interface. (*A*) Ribbon diagram of IFN-γ residues that contact IFN-γBP^{ECTV}. The residues that bury surface area into the interface are colored red. (*B*) Comparison of surface area buried by IFN-γ residues in the IFN-γ/IFN-γBP^{ECTV} (red) or IFN-γ/IFN-γR1 (green) complexes. (*C*) IFN-γBP^{ECTV} residues that bury surface area in the interface (≤3 Å^2, gray; >3 to ≤10 Å^2, blue; >10 to ≤20 Å^2, cyan; >20 to ≤40 Å^2, green; >40 to ≤60 Å^2, yellow; >60 to ≤80 Å^2, orange; >80 Å^2, red). IFN-γ is shown as a magenta ribbon, with the side chains shown in *A*.

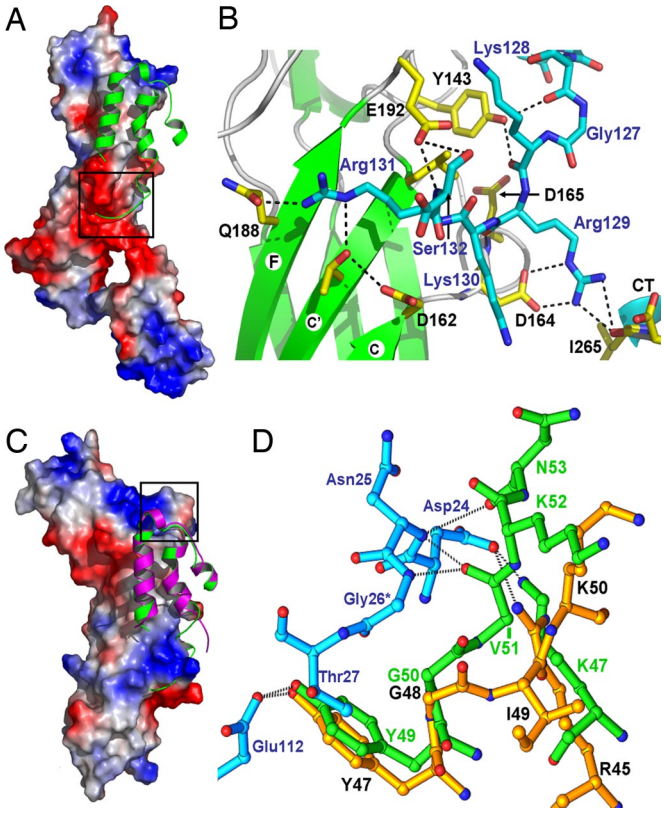

Fig. 5. IFN-γ C terminus and AB loop interactions with IFN-γBP^{ECTV} and IFN-γR1. (*A*) Electrostatic surface potential of IFN-γBP^{ECTV} and the IFN-γ-binding epitope. (*B*) Detailed interactions between the C terminus of IFN-γ (cyan) and IFN-γBP^{ECTV} (yellow) corresponding to the box in *A*. (*C*) Electrostatic surface potential of IFN-γR1 in the same orientation as IFN-γBP^{ECTV} in *A* with IFN-γ from the IFN-γBP^{ECTV} (green) and IFN-γR1 (magenta) complexes. (*D*) Hydrogen bonding in the AB loop regions (boxed region in *C*) of the complexes. IFN-γ side chains are cyan, whereas L2 loop residues from IFN-γBP^{ECTV} and IFN-γR1 are colored gold and green, respectively. Gly-26* denotes the position of Gly-26$^{IFN-\gamma}$, which is deleted in the AB loop of murine IFN-γ.

accessible surface area into each IFN-γ/ IFN-γBP^{ECTV} interface (Fig. 4). In contrast, only 27 IFN-γ residues (>3 Å^2) buried 964 Å^2 of surface area in the IFN-γ/IFN-γR1 complex. Remarkably, 660 Å^2 of the 1,448 Å^2 buried in the complex (≈46% of the total) was contributed by the C terminus. The IFN-γ C terminus also formed 10 hydrogen bonds and/or salt bridge interactions with IFN-γBP^{ECTV} (SI Table 2 and Fig. 5*B*). The binding site was made up predominantly of aspartic acid residues (Asp-162, Asp-164, Asp-165) located on the L6 loop of IFN-γBP^{ECTV}, which was opposite its putative location in IFN-γR1. Residues that form the binding site are conserved in all known orthopoxvirus IFN-γBP sequences, except for Asp-162, which is an asparagine in three of 48 variola sequences. Thus, orthopoxviruses have evolved the same unique mechanism for sequestering the highly conserved C-terminal tail of IFN-γ.

In contrast to the extensive interactions made with the C-terminal tail, IFN-γBP^{ECTV} made fewer contacts with the α-helical domain of IFN-γ than IFN-γR1. Excluding interactions with the IFN-γ C terminus (residues 120–132), IFN-γR1 buried more surface area (939 Å^2) into helices A, B, and F and the AB loop than IFN-γBP^{ECTV} (779 Å^2). Most of the differences occurred in the AB loop region of the interface. In particular, three main chain–main chain hydrogen bonds (Val-51$^{IFN-\gamma R1}$–Asn-25$^{IFN-\gamma}$, Asn-53$^{IFN-\gamma R1}$–Asn-25$^{IFN-\gamma}$, and Val-51$^{IFN-\gamma R1}$–Gly-26$^{IFN-\gamma}$) between the L2 loop of IFN-γR1 and the AB loop of IFN-γ did not occur in the IFN-γBP^{ECTV}/IFN-γ complex because of a two-residue deletion in the IFN-γBP^{ECTV} L2 loop (Fig. 5*D*). Interestingly, Gly-26$^{IFN-\gamma}$, which participates in this IFN-γ/IFN-γR1 hydrogen bonding network, is deleted in the sequence of murine IFN-γ. This suggests that deletions in the IFN-γBP^{ECTV} L2 loop also contributes to the relaxed species specificity of the orthopoxvirus IFN-γBPs.

Discussion

Sequencing of the first poxvirus IFN-γBP in myxoma virus (MT-7) reveals that IFN-γBPs, with the exception of fowlpox virus IFN-γBP (19), contain a stolen copy of the host IFN-γR1 CRHR for its IFN-γ-binding function (20). Whereas the relationship between IFN-γBPs and cellular IFN-γR1 was quickly realized by sequence comparisons, the possible origins and function of the C-terminal sequence of the IFN-γBPs has been more difficult to define. However, structural similarity between the IFN-γBP^{ECTV} C terminus (HTH) and the HTH motif of TFIIA (rmsd, ≈1.6 Å) suggests that the IFN-γBP HTH domain may have originated from a captured host transcription factor oligomerization domain.

The HTH motif assembled four IFN-γBP^{ECTV} chains into an efficient IFN-γ antagonist with an "H"-shaped tetramer structure (Fig. 1*D*). Several studies have confirmed the IFN-γBPs form covalent dimers (11, 21). However, the rod-like covalent IFN-γBP R/T dimers (Fig. 1*B*) did not mimic the IFN-γ/IFN-γR1 complex (Fig. 3*A*) and exhibited significantly reduced ability to antagonize IFN-γ (SI Fig. 7). Instead, high-affinity bivalent interactions between IFN-γBP^{ECTV} and IFN-γ occurred only upon HTH-mediated tetramer formation (Fig. 3 *C* and *D*).

Consistent with the critical location of Phe-250 in the tetramer interface (Fig. 2), SEC analysis (SI Fig. 8) demonstrated the IFN-γBP^{ECTV} Phe250Ala mutant formed dimers rather than tetramers and exhibited a substantially reduced ability to antag-

onize IFN-γ (SI Fig. 7). Interestingly, addition of IFN-γ to IFN-γBP^{ECTV} Phe250Ala reassembled the tetramer (SI Fig. 8). This suggests that the Phe250Ala mutation does not significantly alter the structure of the H3 helix or HTH dimers (Fig. 1*B*). As a result, bivalent interactions between IFN-γ dimers and the CRHRs provided sufficient binding energy to overcome the Phe250Ala tetramer assembly defect. These experiments confirmed the location of the IFN-γBP^{ECTV} tetramer interface and the ability of the Phe250Ala mutant CRHRs to bind IFN-γ.

Residues in the HTH domain appear to be relatively insensitive to alanine point mutations, because only 1 of 14 mutants (Phe250Ala) analyzed thus far disrupts IFN-γBP^{ECTV} tetramer formation. However, mutating IFN-γBP^{ECTV} Phe-261 to proline, rather than to alanine, prevented tetramer assembly (SI Fig. 8). The Phe261Pro mutation may alter the orientation and/or secondary structure of the H3 helix (Fig. 2*A*), which would disrupt the structure of the HTH dimer (Fig. 1*B*) and subsequently prevent tetramer formation (Fig. 1*D*). In contrast to IFN-γBP^{ECTV} Phe250Ala, addition of IFN-γ to the IFN-γBP^{ECTV} Phe261Pro mutant did not reassemble the tetramer (SI Fig. 8). This suggests, despite interactions with IFN-γ through the CRHRs, significant structural changes have occurred in the IFN-γBP^{ECTV} HTH domains that prevent proper dimer formation and tetramer assembly. The inability of the IFN-γBP^{ECTV} Phe261Pro mutant to assemble into a tetramer was reflected by its reduced ability, relative to Phe250Ala, to block IFN-γ activity in the antiviral protection assay (SI Fig. 7).

Structural disruption of the H3 helix/HTH dimer, as described above for IFN-γBP^{ECTV}Phe261Pro, may also explain why deleting three IFN-γBP^{ECTV} C-terminal amino acids (DEL3 mutant, residues Met-264, Leu-265, Asp-266 deleted) disrupts tetramer assembly and IFN-γ binding (9). Two possible mechanisms may explain why the DEL3 mutant disrupts tetramer formation. First, deletion of Met-264 may destabilize the HTH dimer because it buried 117 Å^2 into the dimer interface, compared with 49 and 4 Å^2 for Leu-265 and Asp-266, respectively (Fig. 2). Second, deletion of the three IFN-γBP^{ECTV} C-terminal residues could "unwind" the H3 helix disrupting the HTH dimer structure and tetramer assembly. As observed for IFN-γBP^{ECTV} Phe261Pro, addition of IFN-γ to the DEL3 mutant failed to reassemble the tetramer (SI Fig. 8). Thus, the DEL3 mutation likely causes a significant structural change in the HTH domains, which prevents tetramerization and high affinity IFN-γ binding.

The high sequence identity (>90%) shared among all orthopoxvirus IFN-γBPs, including variola, vaccinia, and monkeypox viruses, suggests they may also adopt tetrameric structures as observed for IFN-γBP^{ECTV}. Although the sequence identity is more limited (≈20%), IFN-γBPs from leporipox, suipox, and capripox genera are also predicted to form tetramers. Our predictions conflict with previous quaternary structure analyses performed on IFN-γBP$^{VACV\text{-}B8R}$ and myxoma virus M-T7 (10, 11). IFN-γBP$^{VACV\text{-}B8R}$, produced in baculovirus infected *Spodoptera frugiperda* cells, exhibits an apparent molecular weight of 68 kDa, corresponding to a dimer when analyzed by sucrose density gradient centrifugation (11). By using analytical ultracentrifugation, an apparent molecular weight of 113 kDa (trimer) has been obtained for M-T7, produced in baby green monkey kidney cells (10). The reason for the discrepancies in quaternary structure remains to be determined. However, the molecular weight obtained for M-T7 differs from the predicted tetramer molecular weight by only ≈15% (132 kDa = 4 × 33 kDa). In addition, Lalani *et al.* report an approximate molecular weight of 175 kDa for M-T7 on gel filtration columns, which is consistent with the molecular weights observed for IFN-γBP^{ECTV} tetramers expressed in CV-1 cells (ref. 10 and SI Fig. 8).

The benefit of assembling IFN-γBP chains into tetramers (Fig. 1*D*), rather than dimers that mimic the cell surface receptor complex (Fig. 3 *A* and *B*), is currently unknown. However, one possibility is that the D2–D2 and HTH motif interactions "lock" the IFN-γBP^{ECTV} CRHRs into optimal orientations for IFN-γ binding. Thus, tetramer formation may pay the entropic cost of ordering two flexible IFN-γR1 CRHRs tethered to a coiled-coil domain upon IFN-γ binding. Tetramerization is a simple and efficient mechanism to lock the CRHRs into an optimal IFN-γ-binding conformation by using only 57 aa. It is doubtful that a "locked" dimeric IFN-γBP^{ECTV} could be achieved without a much larger C-terminal domain requiring additional amino acids.

IFN-γBP^{ECTV} forms an extensive binding site for the positively charged IFN-γ C-terminal tail, residues 128–132 (Figs. 4 and 5). In contrast, the C-terminal tail of IFN-γ is not observed in three different IFN-γR1/IFN-γ crystal structures (14, 16, 17), suggesting that it forms transient interactions with IFN-γR1 and is disordered in the time-averaged structures. Surface plasmon resonance (SPR) studies on murine IFN-γ /IFN-γBP^{ECTV} and human IFN-γ/sIFN-γR1 interactions are consistent with these structural observations (SI Table 3) (9, 22, 23). Specifically, removing the Lys128Arg129Lys130Arg131 sequence (KRKR region; Figs. 4 and 5) from the IFN-γ C-terminal tail, reduces the association rate constant (k_{on} = 7.3 × 10^6 M^{-1} s^{-1}) of the IFN-γ/IFN-γR1 complex ≈4- to 7-fold, with little or no change in the dissociation rate constant (k_{off} ≈ 5 × 10^{-3} s^{-1}). Thus, the positively charged IFN-γ C terminus is critical for the association of IFN-γ and IFN-γR1 but contributes very little to the overall stability of the complex (e.g., k_{off}). The data are consistent with the inability to visualize the IFN-γ C-terminal tail in cellular IFN-γ/IFN-γR1 crystal structures.

The electronegative surface of IFN-γBP^{ECTV} (Fig. 5) suggests the IFN-γ KRKR region is equally critical in the association of the IFN-γ/IFN-γBP^{ECTV} complex despite a small k_{on} constant of 1.2 × 10^5 M^{-1} s^{-1}, which is likely significantly underestimated because of amine coupling of murine IFN-γ to SPR chip surfaces (9). In contrast to IFN-γ/IFN-γR1, the murine IFN-γ/IFN-γBP^{ECTV} dissociation rate constant (k_{off} = 5.7 × 10^{-5} sec^{-1}; SI Table 3) was ≈90-fold smaller (e.g., stronger interaction) than observed in the cellular IFN-γ receptor complex. The slower k_{off} value for the IFN-γ/IFN-γBP^{ECTV} complex is consistent with the extensive interactions observed in the crystal between IFN-γBP^{ECTV} and the C-terminal KRKR region of IFN-γ (Figs. 4 and 5). IFN-γ KRKR/IFN-γBP^{ECTV} contacts emphasize the importance of the IFN-γ C terminus in IFN-γR1 binding, signal transduction (23, 24), and as a conserved recognition motif that facilitates IFN-γBP binding to multiple species of IFN-γ.

In contrast to the extensive interactions with the C terminus, IFN-γBP^{ECTV} formed fewer contacts with the α-helical domain of IFN-γ than IFN-γR1. In particular, IFN-γBP^{ECTV} made fewer hydrogen bonds with the AB loop region of IFN-γ, which has been shown by mutagenesis studies (25) to be an important determinant in the species specificity of IFN-γR1s for their cognate ligands. This suggests IFN-γBP^{ECTV} exhibits relaxed specificity, relative to IFN-γR1, by removing species-specific contacts located in the α-helical regions of IFN-γ while forming extensive interactions with the highly conserved C-terminal tail.

The IFN-γBP^{ECTV} HTH motif represents, to our knowledge, a novel oligomerization domain, which may be important in a number of research, biotechnology, and clinical applications. For example, tetramerization of MHC is currently used for detecting T cell epitopes (26). In addition, protein antagonists of a number of soluble inflammatory molecules have or are being designed. Many of these molecules comprise the extracellular domain of a cell surface receptor attached to an antibody Fc domain. For example, etanercept, a TNF receptor Fc fusion protein, is a potent inhibitor of TNF-α used to control rheumatoid arthritis (27). In addition, antagonists of IFN-γ have recently shown positive results in the treatment of inflammatory bowel disease (28). Thus, further study of the IFN-γBP family, and their HTH

motifs, has tremendous potential in furthering scientific discovery and improving human health.

Methods

Expression and Purification. Human IFN-γ residues 1–138, containing a C-terminal AviTag (Avidity), were coexpressed with biotin ligase (BirA) in BL21 (DE3) cells. Inclusion bodies were solubilized in 100 mM Tris, pH 8.0, and 6.0 M guanidine HCl and clarified by centrifugation at 21,000 × *g* for 20 min. Biotinylated IFN-γ (hIFN-γAvtB) was refolded in a solution containing 100 mM Tris, pH 8.0, 2.5 mM EDTA, 500 mM L-arginine, and 10 mM benzamidine at 4°C with rapid stirring.

The full-length IFN-γBP^{ECTV} gene was cloned into the KpnI and XhoI sites of the drosophila expression vector pMT/V5-HisA (Invitrogen) and cotransfected into the *D. melanogaster* S2 cells along with the pCpHygro selection plasmid (Invitrogen) by using calcium phosphate precipitation. Stable transfectants were grown in Insect-Express serum-free media (Cambrex) to a density of 5×10^6 cells per milliliter, and IFN-γBP^{ECTV} expression was induced by the addition of Cu_2SO_4.

IFN-γBP^{ECTV} was purified by affinity chromatography by using IFN-γAvtB attached to monomeric–avidin agarose (Pierce). The IFN-γBP^{ECTV} /IFN-γAvtB complex was eluted from the column with 100 mM glycine, pH 2.8, and immediately neutralized with 1.0 M Tris, pH 7.0. The eluted IFN-γBP^{ECTV}/IFN-γAvtB complex was further purified by gel filtration chromatography by using a Superdex 200 column (GE Healthcare) in 100 mM Hepes, pH 8.0, 150 mM NaCl, and 2.5 mM EDTA. Fractions containing the IFN-γBP^{ECTV}/IFN-γAvtB complex were pooled and concentrated to 10 mg/ml for crystallization studies.

Crystallization, Structure Determination, and Refinement. Crystals of the IFN-γBP^{ECTV} /IFN-γAvtB were grown by hanging-drop vapor diffusion from solutions of 0.8 M NaH_2PO_4/0.8 M KH_2PO_4 in 100 mM Hepes buffer, pH 7.4, at 25°C. Crystals suitable for data collection were obtained after 3 weeks and cryopreserved in solutions of 2.2 M NaH_2PO_4 in 100 mM Hepes buffer, pH 4.3, and 15% glycerol. A low-temperature (100° K) native dataset was collected on SER-CAT beamline 22-ID at the Advanced Photon Source (Argonne National Laboratory).

The position of IFN-γ in the IFN-γAvtB/IFN-γBP^{ECTV} crystals was identified by using MolRep (CCP4) (29). Calculated phases were modified at 2.2-Å resolution by using the solvent leveling–flipping routines in CNS (30) combined with a solvent mask initially derived from the IFN-γ/IFN-γR1 structure. The modified phases were imported to Arp-Warp (31), resulting in a model that was 95% complete. Additional refinement was performed with CNS (version 1.1) by using the maximum likelihood target function (30). Before all building and refinement, 5% of the data were randomly omitted for monitoring the free *R* factor (R_{free}). Manual rebuilding was performed by using the graphics program O (32). The final refinement statistics are presented in SI Table 1. Buried surface area was calculated by using AREAIMOL in CCP4 (29). Ribbons (33) and PyMOL (DeLano Scientific) were used for figure generation.

Antiviral Protection Assay and Size Exclusion Chromatography. Antiviral protection assays were performed on murine L929 cells as described previously (9). IFN-γBP^{ECTV} and mutants were injected onto a calibrated superdex 200 column, and protein fractions were detected by Western blotting (9).

ACKNOWLEDGMENTS. We thank Dr. Michael Boyle for expert advice in protein purification. This work was funded by National Institutes of Health Grants AI47300 (to M.R.W.) and N01-AI-15436 (to R.M.B.) and a University of Alabama at Birmingham Center for Emerging Infections and Emergency Preparedness pilot grant (to M.R.W.). A.A.N. was supported, in part, by an American Heart Association predoctoral fellowship. Use of the APS was supported by U.S. Department of Energy Contract No. W-31-109-Eng-38.

1. Esteban DJ, Buller RM (2005) Ectromelia virus: The causative agent of mousepox. *J Gen Virol* 86:2645–2659.
2. Seet BT, *et al.* (2003) Poxviruses and immune evasion. *Annu Rev Immunol* 21:377–423.
3. Alcami A (2003) Viral mimicry of cytokines, chemokines and their receptors. *Nat Rev Immunol* 3:36–50.
4. Karupiah G, *et al.* (1993) Importance of interferons in recovery from mousepox. *J Virol* 67:4214–4226.
5. Chaudhri G, *et al.* (2004) Polarized type 1 cytokine response and cell-mediated immunity determine genetic resistance to mousepox. *Proc Natl Acad Sci USA* 101:9057–9062.
6. Sakala IG, *et al.* (2007) Poxvirus encoded interferon-gamma binding protein dampens the host immune response to infection. *J Virol.* 81:3346–3353.
7. Mossman K, Upton C, Buller RM, McFadden G (1995) Species specificity of ectromelia virus and vaccinia virus interferon-gamma binding proteins. *Virology* 208:762–769.
8. Alcami A, Smith GL (1995) Vaccinia, cowpox, and camelpox viruses encode soluble gamma interferon receptors with novel broad species specificity. *J Virol* 69:4633–4639.
9. Nuara AA, *et al.* (2006) The unique C termini of orthopoxvirus gamma interferon binding proteins are essential for ligand binding. *J Virol* 80:10675–10682.
10. Lalani AS, *et al.* (1997) The purified myxoma virus gamma interferon receptor homolog M-T7 interacts with the heparin-binding domains of chemokines. *J Virol* 71:4356–4363.
11. Alcami A, Smith GL (2002) The vaccinia virus soluble interferon-gamma receptor is a homodimer. *J Gen Virol* 83:545–549.
12. Tan S, Hunziker Y, Sargent DF, Richmond TJ (1996) Crystal structure of a yeast TFIIA/TBP/DNA complex. *Nature* 381:127–151.
13. Geiger JH, Hahn S, Lee S, Sigler PB (1996) Crystal structure of the yeast TFIIA/TBP/DNA complex. *Science* 272:830–836.
14. Walter MR, *et al.* (1995) Crystal structure of a complex between interferon-gamma and its soluble high-affinity receptor. *Nature* 376:230–235.
15. O'Shea EK, Klemm JD, Kim PS, Alber T (1991) X-ray structure of the GCN4 leucine zipper, a two-stranded, parallel coiled coil. *Science* 254:539–544.
16. Thiel DJ, *et al.* (2000) Observation of an unexpected third receptor molecule in the crystal structure of human interferon-gamma receptor complex. *Structure Fold Des* 8:927–936.
17. Randal M, Kossiakoff AA (2001) The structure and activity of a monomeric interferon-gamma:alpha-chain receptor signaling complex. *Structure (London)* 9:155–163.
18. Nuara AA, Buller RM, Bai H (2007) Identification of residues in the ectromelia virus gamma interferon-binding protein involved in expanded species specificity. *J Gen Virol* 88:51–60.
19. Puehler F, *et al.* (2003) An interferon-gamma-binding protein of novel structure encoded by the fowlpox virus. *J Biol Chem* 278:6905–6911.
20. Upton C, Mossman K, McFadden G (1992) Encoding of a homolog of the IFN-gamma receptor by myxoma virus. *Science* 258:1369–1372.
21. Bai H, *et al.* (2005) Biosynthesis of the IFN-gamma binding protein of ectromelia virus, the causative agent of mousepox. *Virology* 334:41–50.
22. Sadir R, Forest E, Lortat-Jacob H (1998) The heparan sulfate binding sequence of interferon-gamma increased the on rate of the interferon-gamma-interferon-gamma receptor complex formation. *J Biol Chem* 273:10919–10925.
23. Haelewyn J, *et al.* (1997) Interaction of truncated human interferon gamma variants with the interferon gamma receptor: Crucial importance of Arg-129. *Biochem J* 324(Pt 2):591–595.
24. Lundell D, *et al.* (1991) The carboxyl-terminal region of human interferon gamma is important for biological activity: Mutagenic and NMR analysis. *Protein Eng* 4:335–341.
25. Lundell D, *et al.* (1994) Importance of the loop connecting A, B helices of human interferon-gamma in recognition by interferon-gamma receptor. *J Biol Chem* 269:16159–16162.
26. Mallone R, Nepom GT (2004) MHC class II tetramers and the pursuit of antigen-specific T cells: Define, deviate, delete. *Clin Immunol* 110:232–242.
27. Cole P, Rabasseda X (2004) The soluble tumor necrosis factor receptor etanercept: A new strategy for the treatment of autoimmune rheumatic disease. *Drugs Today (Barcelona)* 40:281–324.
28. Ghosh S, Chaudhary R, Carpani M, Playford R (2006) Interfering with interferons in inflammatory bowel disease. *Gut* 55:1071–1073.
29. Winn MD, *et al.* (2002) Ongoing developments in CCP4 for high-throughput structure determination. *Acta Crystallogr D Biol Crystallogr* 58:1929–1936.
30. Brunger AT, *et al.* (1998) Crystallography & NMR system: A new software suite for macromolecular structure determination. *Acta Crystallogr D Biol Crystallogr* 54(Pt 5):905–921.
31. Cohen SX, *et al.* (2004) Towards complete validated models in the next generation of ARP/wARP. *Acta Crystallogr D Biol Crystallogr* 60:2222–2229.
32. Jones TA, Zou JY, Cowan SW, Kjeldgaard M (1991) Improved methods for building protein models in electron density maps and the location of errors in these models. *Acta Crystallogr D Biol Crystallogr* 47:283–290.
33. Carson M (1997) Ribbons. *Methods Enzymolology* 277:493–505.